The Origins of High Hardening and Low Ductility in Magnesium

Zhaoxuan Wu[1,2] and W. A. Curtin[1,*]

[1]Institute of Mechanical Engineering,

École Polytechnique Fédérale de Lausanne, Lausanne CH-1015, Switzerland

[2]Institute of High Performance Computing,

1 Fusionopolis Way, #16-16 Connexis, Singapore 138632

Abstract

Magnesium is the ultimate lightweight structural metal but exhibits low ductility connected to unusual, mechanistically-unexplained, dislocation/plasticity phenomena, which make it difficult to form and use in energy-saving lightweight structures. Here, long-time molecular dynamics simulations using a DFT-validated interatomic potential reveal the fundamental origins of the previously-unexplained phenomena and show a clear path toward design of new ductile magnesium alloys. The key $\langle c + a \rangle$ dislocation is metastable on easy-glide pyramidal II planes and undergoes a thermally-activated, stress-dependent transition to one of three lower-energy, basal-dissociated immobile dislocation structures, which (i) cannot contribute to plastic straining and (ii) serve as strong obstacles to the motion of all other dislocations. The transition is intrinsic to magnesium, driven by reduction in dislocation energy and predicted to occur at very high frequency at room temperature, thus eliminating all major dislocation slip systems able to contribute to c-axis strain and leading to its low ductility. Enhancing ductility can thus be achieved by delaying, in time and temperature, the transition from the easy-glide metastable dislocation to the immobile basal-dissociated structures, and our results provide the underlying insights needed to guide the design of ductile magnesium alloys.

---

*Corresponding author: william.curtin@epfl.ch

Developing lightweight structural metal is a crucial step on the path toward reduced energy consumption in many industries, especially automotive[1,2] and aerospace[3]. Magnesium (Mg) is the ultimate lightweight metal, with a density 23% that of steel and 66% that of aluminum, and so has tremendous potential to achieve energy efficiency[4]. In spite of this tantalizing property, Mg generally exhibits low ductility, insufficient for the forming and performance of structural components. The low ductility is associated with the inability of hexagonally-close-packed (hcp) Mg to deform plastically in the crystallographic $\langle c \rangle$ direction, which is accomplished primarily by dislocation glide on the pyramidal II plane with the $\langle c + a \rangle$ Burgers vector[5] (see Fig. 1). Experiments reveal a range of unusual, confounding, conflicting, and mechanistically-unexplained phenomena connected to $\langle c+a \rangle$ dislocations that coincide with the inability of Mg to achieve high plastic strains[6]. Uncovering and controlling the fundamental behavior of $\langle c + a \rangle$ dislocations is thus the key issue in Mg, and any solution would catapult Mg science, technology, and applications forward. Success would enable, for instance, lightweight automobiles that would consume less energy, independent of the energy source, and thus act as a multiplier for many other energy-reduction strategies.

Due to its critical importance and promise, observing and understanding $\langle c + a \rangle$ slip has been extensively studied over five decades[7–10], and is accelerating recently[11–14]. In Mg single crystals, $\langle c+a \rangle$ slip occurs predominantly on the pyramidal II (Pyr. II) system, and measurements show that Pyr. II $\langle c + a \rangle$ dislocations can glide at low stresses of ∼20 MPa at low temperatures[15] (77-133K). However, TEM studies frequently find $\langle c+a \rangle$ dislocations lying, mysteriously, along *basal* planes and coexisting with $\langle c \rangle$ and $\langle a \rangle$ dislocations[9,16–19]. Under **c**-axis compression, single crystal Mg also exhibits a rapid increase in stress with increasing strain, i.e. high work hardening[9,15,18,19], and fractures at low strains at temperatures up to 500 K[9,15,19]. New work shows the formation of a very high density of $\langle c + a \rangle$ dislocation loops also dissociated on, and lying on, the *basal* planes[14], with similar observations dating back fifty years[7,8,20]. Many mechanisms have been proposed, all of which invoke extrinsic effects such as "heating" by the electron beam[8], vacancy and self-interstitial precipitation[21], and dislocation obstacles of "unknown" nature[7]. Also surprisingly, when loaded at slow strain rates (∼10^{-1}-10^{-5}/s), and particularly under compression, the yield strengths of both single crystal Mg[8,15–17] and polycrystal Mg alloys[22,23] show an increasing strength with increasing temperature, i.e. anomalous temperature dependence, within a certain temperature range. This behavior is hypothesized as due to decomposition of the $\langle c + a \rangle$ dislocation into $\langle c \rangle$ and $\langle a \rangle$ [17], which is supported by TEM [16,21] where junction pairs of $\langle c \rangle$, $\langle a \rangle$, and $\langle c + a \rangle$ dislocations were

found. However, no decomposition process has been directly observed. It has also been proposed that the junctions may be formed by reactions of $\langle c \rangle$ and $\langle a \rangle$ dislocations[24]. The $\langle c \rangle$ dislocation is also unusual because it too lies on the *basal* plane[8,12,25]. Overall, how $\langle c + a \rangle$ and $\langle c \rangle$ dislocations can come to lie on the basal plane is the topic of speculation, confusion, and sometimes disbelief. Nor is there any understanding of why the behavior of $\langle c + a \rangle$ dislocations varies widely over a range of loading conditions, single-crystal orientations, polycrystalline texture, and temperature. Here, we provide an explanation for all of these unusual observed phenomena that is entirely intrinsic to hcp Mg.

Mechanisms of $\langle c + a \rangle$ dislocation transition

We first show the transition of the Pyr. II $\langle c + a \rangle$ edge dislocation into various basal-oriented structures using MD simulations (see Methods). Properties of the screw dislocation are not directly relevant, and are presented in Extended Data Figs. 1 and 7. An initial $\langle c + a \rangle$ edge dislocation core starts on the Pyr. II glide plane and dissociates into $1/2\langle c + a \rangle$ $+1/2\langle c + a \rangle$ on this plane, a structure in good agreement with DFT[26] (see Methods and Ref[5] for all the Burgers vector notations). We then execute long-time MD at elevated temperatures $T = 500, 600, 700$ K to accelerate any thermally activated processes, and under various applied stresses normal to the glide plane. As shown in Fig. 1, the initial $\langle c + a \rangle$ core is *metastable* and transforms into one of three new dislocation structures. The transition into the final state is always preceded by an intermediate state where a partial $\langle a \rangle$ (Shockley type) dislocation is nucleated on the basal plane and glides away from the initial dislocation with a trailing basal I_2 intrinsic stacking fault. Since the time to achieve this intermediate state (indicated in Fig. 1) is much longer than the subsequent transition to any of the final states, the transition into this intermediate state is the kinetically-limiting step in the overall process. An applied normal stress exerts a resolved shear stress on the basal plane that determines the glide of the partial $\langle a \rangle$ dislocation, which in turn determines the final structure. The frequencies of occurrence of the various final dislocation structures as a function of load are shown in Extended Data Fig. 2.

Figure 1a shows the transition that predominates at zero/low applied stress. The newly-nucleated partial $\langle a \rangle$ stays close to the original nucleation site and another partial $\langle a \rangle$ dislocation is then nucleated from the other half $\langle c + a \rangle$ dislocation. The two remaining partials then "climb" in opposite directions to form a new $\langle c + a \rangle$ core dissociated on the *basal* plane and separated

figure_1.pdf

Figure 1: Dissociation of the easy glide Pyr. II edge $\langle \mathbf{c}+\mathbf{a} \rangle$ dislocation. The $\langle \mathbf{c}+\mathbf{a} \rangle$ dislocation transforms into basal dissociated products as observed during long-time MD simulations, for (a) zero, (b) moderate, and (c) high compressive stresses normal to the Pyr. II plane. All cases start from the same dislocation (1st image) and show a distinct thermally-activated intermediate state (2nd image) before undergoing a rapid intrinsic "climb-like" dissociation onto the basal plane. The final core structure (last image) depends on the applied load, with increasing applied load able to drive an $\langle \mathbf{a} \rangle$ or partial $\langle \mathbf{a} \rangle$ dislocation away from the $\langle \mathbf{c}+\mathbf{a} \rangle$ core. $\bar{t}$ is the mean waiting time to reach the intermediate state shown. Dislocation cores are indicated by the symbol "⊥". Atoms in this figure and subsequent ones are colored based on common neighbor analysis: blue = hexagonally-close-packed; green = face-centered-cubic; purple = body-centered-cubic; yellow = all others; dislocation core atoms thus appear predominantly as yellow.

4

Figure 2: $\langle \mathbf{c} + \mathbf{a} \rangle$ dislocation core structure comparison. Superposition of the atomistic structure of one $\langle \mathbf{1/2c} + \mathbf{p} \rangle$ core as computed by MD (open circles) and the HAADF-STEM image of the same core[14], for which bright spots indicate well-defined columns of atoms through the thickness of the experimental specimen; a Burgers loop indicating the $\langle \mathbf{1/2c} + \mathbf{p} \rangle$ Burgers vector is shown for both images.

by a basal I_1 stacking fault[5]. The "climb"-like transition is atomistically complicated, involving significant atomic motions within the core region, but does not involve any vacancy/interstitial diffusion from the surrounding bulk because the simulation contains zero vacancies or interstitials (see Methods and Extended Data Fig. 3). The core spreading on the basal plane is driven by the repelling force between the two partials, but the spreading is kinetically difficult because further climb would presumably require some sort of vacancy/interstitial pair formation and transport (see Methods). This final dislocation core is the one recently observed in HAADF STEM[14] and previously [8,11]. Figure 2 shows a superposition of the atomic images from MD (projected into the plane of view perpendicular to the dislocation line) and from HAADF (which show spots due to diffraction from aligned columns of atoms), for one of the two basal-oriented $\langle \mathbf{c} + \mathbf{a} \rangle$ partial dislocations ($\langle \mathbf{1/2c} + \mathbf{p} \rangle$ where $\mathbf{p}$ is the Burgers vector of the Shockley partial $\langle \mathbf{a} \rangle$ dislocation) with the I_1 stacking fault emerging from it. Good agreement can be seen outside the core region. In the core region, the MD results show complex variations in atomic position along the dislocation line which is consistent with the absence of clear spots in the HAADF STEM that suggest an absence of structural order.

Figure 1b shows the transition that occurs mainly at intermediate applied loads. In this case, the first nucleated leading partial $\langle \mathbf{a} \rangle$ glides away, leaving behind a wide I_2 stacking fault and a $1/2\langle \mathbf{c} \rangle$ $+ d\alpha$ dislocation. The other half $\langle \mathbf{c} + \mathbf{a} \rangle$ on the Pyr. II plane then reacts with the residual dislocation to form another new "climb-dissociated" dislocation with Burgers vector of $1/2\langle \mathbf{c} \rangle + B'A_0$. If the applied stress is then reduced, this core transforms into the previous core because the partial $\langle \mathbf{a} \rangle$

is pulled back to the main dislocation. Figure 1c shows the transition that predominates at higher loads. In this case, the Pyr. II $\langle \mathbf{c} + \mathbf{a} \rangle$ decomposes into $\langle \mathbf{c} \rangle$ and $\langle \mathbf{a} \rangle$ dislocations by nucleating a trailing partial $\langle \mathbf{a} \rangle$ behind the initial leading partial $\langle \mathbf{a} \rangle$. The full $\langle \mathbf{a} \rangle$ then glides away, driven by the high applied resolved shear stress, leaving behind a $\langle \mathbf{c} \rangle$ dislocation. The $\langle \mathbf{c} \rangle$ then also "climb-dissociates" along the basal plane into two partial $\langle \mathbf{c} \rangle$ separated by a basal extrinsic stacking fault, consistent with TEM observations[25] and HAADF STEM[12].

Dislocation transition rate and energy barrier

Figure 3: Thermally-activated mean transition time and energy barrier for the Pyr. II to basal plane transformation, at three temperatures. (a) Mean transition times versus applied normal load, as measured in MD for the dissociation events shown in Fig. 1; (b) Energy barrier for the thermally activated transitions, showing a small dependence on temperature and normal stress. Error bars indicate the confidence intervals of the mean transition time and energy barrier. Open, half-filled and quarter-filled circles indicate (nearly identical) results obtained for larger simulation cells and different boundary conditions.

The $\langle \mathbf{c} + \mathbf{a} \rangle$ dislocation transformations are *thermally activated* processes. Figure 3a shows the measured mean transition time $\bar{t}$ versus stress and temperature for this random process. The $\bar{t}$ depends on temperature and, weakly, on stress. Simulation cell size and boundary conditions have insignificant effects on the measured transition rate (see Methods). The mean transition rate $R = 1/\bar{t}$ can be related to the normal-stress-dependent transition energy barrier $\Delta E(\sigma_{norm})$ using the Arrhenius law $R = \nu_0 \exp^{-\Delta E(\sigma_{norm})/kT}$, where ν_0 is an attempt frequency. Estimating $\nu_0 =$

10^{13}/s, the energy barrier versus normal applied stress is shown in Fig. 3b. Overall, the energy barrier is ∼0.5 eV. This yields a fast transition rate of ∼10^5/s at 300K and a very slow rate of ∼10^{-4}/s at 150K, consistent with the observation of anomalous hardening only above ∼150K[16,17]. Preliminary nudged elastic band[27,28] calculations of the zero temperature activation barrier yield an energy barrier of ∼0.6 eV in good agreement with the estimates in Fig. 3 (see Methods). The applied stress has a weak asymmetrical effect on nucleation because it influences the barrier by exerting a stress that moves the first partial $\langle \mathbf{a} \rangle$ dislocation away (compressive) or toward (tensile) the original $\langle \mathbf{c} + \mathbf{a} \rangle$ dislocation.

Dislocation energy

The observed transitions are driven by a reduction in total dislocation energy: all the new dislocations have lower energy than the easy-glide Pyr. II $\langle \mathbf{c} + \mathbf{a} \rangle$. The total dislocation energy per unit length within a cylindrical region of radius r centered at the dislocation core can be written as $E_{tot} = E_{struc} + K \ln (r/r_{min})$ for $r > r_{min}$ (see Extended Data Fig. 7a). Here, E_{struc} is the dislocation energy within a minimum radius r_{min} around the core region that contains all of the energy associated with the specific structure, such as the core energy, stacking fault energy, interactions among these structures, and near-field elastic energy. Conversely, the second term $K \ln (r/r_{min})$ is the additional elastic energy between r_{min} and radius r from the core region, which captures the elastic energy outside of the core region. The constant K is completely determined by the anisotropic elastic constants, Burgers vector $\mathbf{b}$, and dislocation line direction. Here, all the $\langle \mathbf{c} + \mathbf{a} \rangle$ dislocations and total products have the same K, $b = |\mathbf{c} + \mathbf{a}|$ Burgers vector, and line direction. Therefore, the total energy *difference* between any two structures can be measured directly by the difference in their total energies E_{tot} measured at large distances $r > r_{min}$ from the complex core region[5]. Figure 4a shows E_{tot} vs $\ln (r/r_{min})$ for $r_{min} = 6b$ calculated atomistically for the three localized edge $\langle \mathbf{c} + \mathbf{a} \rangle$ type dislocations found here. All three curves are parallel, as expected for $E_{tot}(r > r_{min})$, and the energy *differences* are precisely the differences in E_{struc} between the different structures. The initial $\langle \mathbf{c} + \mathbf{a} \rangle$ dislocation on the Pyr. II plane has the largest energy per unit length and the $\langle \mathbf{c} + \mathbf{a} \rangle$ dislocation dissociated on the basal plane has the smallest energy, 0.3 eV/Å lower, and is the most stable at zero applied stress. The $\langle \mathbf{c} \rangle + \langle \mathbf{a} \rangle$ dislocation remaining in close proximity has an intermediate energy and is thus also stable relative to the easy-glide structure. In fact, while not shown, a related calculation can be performed to demonstrate that even the
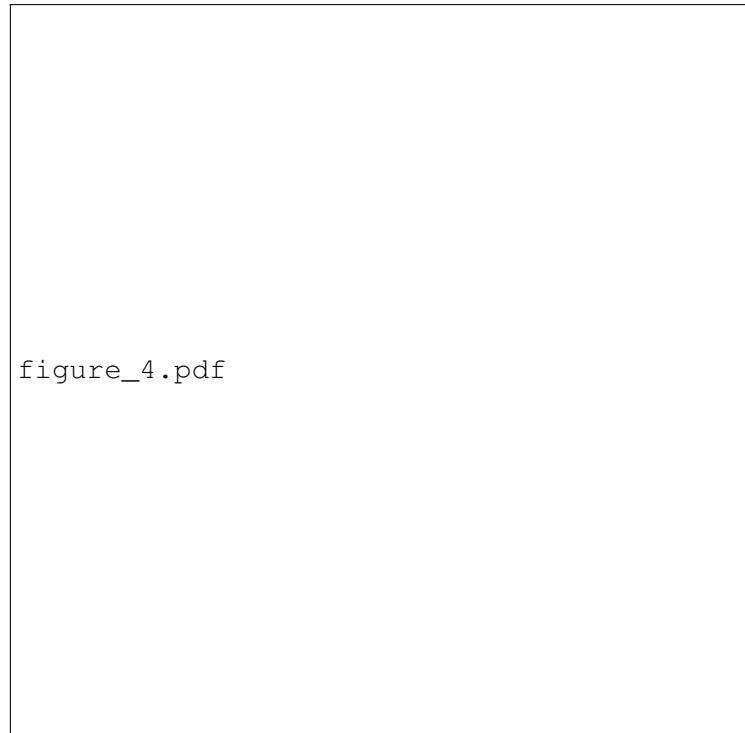
Figure 4: Dislocation energy versus dislocation structure. (a) Total energy of the various $\langle \mathbf{c}+\mathbf{a}\rangle$ dislocations within a cylindrical region of radius $r > r_{min} \approx 6b$ for the three $\langle \mathbf{c}+\mathbf{a}\rangle$ edge dislocations on the pyramidal II plane, edge $\langle \mathbf{c}\rangle$ and $\langle \mathbf{a}\rangle$ in close proximity, and $\langle \mathbf{c}+\mathbf{a}\rangle$ edge dislocation climb-dissociated on basal plane. Here, b is the magnitude of the $\langle \mathbf{c}+\mathbf{a}\rangle$ dislocation Burgers vector. The difference in energies among the three different dislocation structures are equal to the constant differences among the energies vs. r, as expected by elasticity theory. (b) Dislocation core structures corresponding to the energies shown in (a) as computed at zero temperature.

case of $\langle \mathbf{c}\rangle$ and $\langle \mathbf{a}\rangle$ separated to infinity has a lower total energy than the easy glide core, although higher than the $\langle \mathbf{c}\rangle + \langle \mathbf{a}\rangle$ in close proximity, indicating that short-range interactions between the $\langle \mathbf{c}\rangle$ and $\langle \mathbf{a}\rangle$ dislocations reduce the overall energy relative to well-separated dislocations. There is thus an energy barrier for driving the $\langle \mathbf{a}\rangle$ dislocation away from the $\langle \mathbf{c}\rangle$ dislocation.

The relative order of the edge dislocation energies rationalizes the simulations and various experimental observations. Under zero or low applied normal stress, the preferred dislocation transition is the lowest energy "climb-dissociated" $\langle \mathbf{c}+\mathbf{a}\rangle$ structure on the basal plane. This is consistent with experimental observations in single crystal **c**-axis compression tests, where the resolved shear stress on the basal plane is negligible and a high density of $\langle \mathbf{c}+\mathbf{a}\rangle$ loops/dislocations dissociated on basal planes[14,19] or aligned with basal planes[9] are observed. When there is a re-

8

solved stress τ on the basal plane, there is energy gained by the work done by the applied field in moving the partial and/or full $\langle \mathbf{a} \rangle$ away from the $\langle \mathbf{c} \rangle$ dislocation. When the full or partial $\langle \mathbf{a} \rangle$ has moved a distance l, the total energy reduction per unit length is $\Delta E = \tau a l$ for the $\langle \mathbf{a} \rangle$ dislocation and $\Delta E = \tau a l / 2 - \gamma_{I_2} l$ for the partial $\langle \mathbf{a} \rangle$, where γ_{I_2} is the I_2 stacking fault energy ($\sim$20-30 mJ/m^2). These two cores can thus have the lowest total energy at sufficiently large applied τ. This is consistent with experimental observations in polycrystal Mg[21], where resolved shear stresses exist on the basal planes in most grains and $\langle \mathbf{c} \rangle$ and $\langle \mathbf{a} \rangle$ dislocations/junctions are more commonly seen as compared to $\langle \mathbf{c} + \mathbf{a} \rangle$ basal loops.

Critical resolved shear stresses for dislocation glide

The three transformed cores shown in Fig. 1 are essentially immobile, as expected due to their "climb dissociation" onto the (non-glide) basal planes. Figure 5 shows the motion of the various dislocations under an applied resolved shear stress on the Pyr. II plane (a-d) and prism plane (e) at 300 K, as obtained via MD simulations (see Methods). The initial $\langle \mathbf{c} + \mathbf{a} \rangle$ dislocation on the Pyr. II plane glides at stresses of $\sim$11 MPa. All of the basal-dissociated dislocations are immobile up to stresses more than 30$\times$ the Pyr. II glide stress (see Extended Data Fig. 8 for non-Schmid effect); only the $\langle \mathbf{a} \rangle$ can glide away at 119 MPa, as discussed above, leaving the immobile $\langle \mathbf{c} \rangle$. A stress of 430 MPa is needed to recombine the $\langle \mathbf{a} \rangle$ and $\langle \mathbf{c} \rangle$ into the $\langle \mathbf{c} + \mathbf{a} \rangle$, indicating a high energy barrier for this reverse reaction so that this proposed mechanism for creation of $\langle \mathbf{c} + \mathbf{a} \rangle$ is unlikely[24].

Origin of low ductility and high strain hardening

The time-dependent thermal activation of the easy-glide Pyr. II $\langle \mathbf{c} + \mathbf{a} \rangle$ to immobile lower-energy, basal-oriented $\langle \mathbf{c} + \mathbf{a} \rangle$ and $\langle \mathbf{c} \rangle$ dislocations explains the low ductility of Mg. Generalized plasticity requires the operation of at least 5 independent slip systems[5]. Mg cannot sustain dislocation slip in the crystallographic $\langle \mathbf{c} \rangle$ direction because the necessary $\langle \mathbf{c} + \mathbf{a} \rangle$ and $\langle \mathbf{c} \rangle$ dislocations transform to immobile dislocation structures. Thus, only twinning remains to provide some deformation in the $\langle \mathbf{c} \rangle$, and the plastic strain due to twinning is very small (at most, $\sim$7%). Grains in a polycrystal can thus mainly slip only in the $\langle \mathbf{a} \rangle$ direction, and grains oriented favorably for $\langle \mathbf{c} + \mathbf{a} \rangle$ slip are effectively rigid. High constraint stresses rapidly develop, leading to the early onset of

figure_5.pdf

Figure 5: Glide behavior of the various dislocations under applied resolved shear stresses (directions indicated) at 300K. (a) Easy glide Pyr. II $\langle \mathbf{c} + \mathbf{a} \rangle$, with glide starting at ∼11 MPa; (b) Basal-dissociated $\langle \mathbf{c} + \mathbf{a} \rangle$, with glide starting at very high stresses ∼330 MPa; (c) $\langle \mathbf{a} \rangle$ dislocation glide away from the remaining $\langle \mathbf{c} + \mathbf{a} \rangle$ product at ∼119 MPa leaving an immobile $\langle \mathbf{c} \rangle$; (d) Reaction of $\langle \mathbf{a} \rangle$ and $\langle \mathbf{c} \rangle$ forming the basal $\langle \mathbf{c} + \mathbf{a} \rangle$ dislocation for resolved shear of ∼ 430 MPa in the reverse direction; (e) Absence of glide for the basal-dissociated $\langle \mathbf{c} \rangle$ up to ∼464 MPa, where nucleation of a partial $\langle \mathbf{a} \rangle$ dislocation occurs.

fracture and low ductility.

Low ductility is also driven by high hardening rates, as measured in Mg, particularly for single crystals or textured polycrystals oriented for $\langle \mathbf{c} + \mathbf{a} \rangle$ slip. The immobile dislocations do not contribute to plastic straining and instead act as "forest" dislocations that impede the motion of dislocations on all the easy-glide/slip systems. Plastic flow on slip system α, (α = basal, prism, twin, pyramidal) is controlled by the densities of mobile dislocations ρ_m^α and "forest" dislocations ρ_f^α impeding slip on each slip system. The contribution to the total plastic strain rate from slip system α is then

$$\dot{\epsilon}_p^\alpha = \frac{\rho_m^\alpha b^\alpha}{\sqrt{\sum_{\alpha'} \rho_f^{\alpha'}}} R_{esc} \tag{1}$$

10

where

$$R_{esc} = \nu_{esc} \exp\left\{-\frac{\Delta G_0}{kT}\left[1 - \left(\frac{\tau^\alpha}{\tau^\alpha_{crit}}\right)^p\right]^q\right\} \tag{2}$$

is the rate of thermally-activated escape of the α dislocations past the forest obstacles[29]. The parameters in Eqn. 2 (attempt frequency ν_{esc}, zero-stress activation energy G_0, and exponents p and q characterizing the activation energy profile) are not important for the general discussion here. The key quantities are the applied resolved shear stress τ^α acting on the dislocations and the zero-temperature strength or critical flow stress τ^α_{crit} required to overcome the energy barrier without thermal activation. τ^α_{crit} is due to the forest obstacles, and so is related to the dislocation densities in all slip systems α' including α itself as[30,31]

$$\tau^\alpha_{crit} = \mu b^\alpha \sqrt{\sum_{\alpha'} A^{\alpha\alpha'} \rho^{\alpha'}_f} \tag{3}$$

where μ is the shear modulus (ignoring elastic anisotropy) and $A^{\alpha\alpha'}$ is the matrix of interaction strengths between slip systems α and α'. Around room temperature, the fast transition of easy-glide $\langle c + a \rangle$ dislocations into immobile basal-dissociated $\langle c + a \rangle$ or $\langle c \rangle$ dislocations acts to (i) rapidly decrease the density of mobile $\langle c + a \rangle$ dislocations ρ_m and (ii) rapidly increase the density of immobile/forest dislocations ρ_f affecting all glide systems. For all slip systems, the most important effect is the exponential decrease in the escape rate (Eqn. 2) due to the increased critical strengths on all slip systems (Eqn. 3) due, in turn, to the increased forest density associated with the transformed $\langle c + a \rangle$ dislocations. The increased forest density also decreases the slip rate directly in Eqn. 1. Therefore, constant-strain-rate experiments show a very rapid increase in the applied stress required to sustain the imposed loading rate, and thus a rapidly increasing hardening rate in the stress-strain curve. High stresses then drive fracture, which cannot be resisted by plastic flow, and the ductility is thus limited.

Strain hardening is particularly dramatically enhanced in crystals oriented preferentially for $\langle c + a \rangle$ slip. In such an orientation, previously-transformed $\langle c + a \rangle$ dislocations on the basal planes block subsequent easy-glide Pyr. II $\langle c + a \rangle$ dislocations at their leading edge segments and drive those dislocations to evolve into long straight segments with pure edge character. These dislocations then transform into immobile dislocations, thus forming immobile dislocation pile-ups. There is thus a feedback process: the rate of transformation increases with increasing immobile dislocation density while the immobile dislocation density increases due to the increasing number of transformations. This is observed in single crystal Mg c-axis compression tests[9,14,19] where

11

the exceptionally high measured work hardening is accompanied by the observation of a rapid increase of straight $\langle c+a \rangle$ dislocations and also loops (density of $\sim 10^{20}$ m^{-3} at 1% plastic strain[14]). In fact, when $\langle c+a \rangle$ dislocations are observed in TEM[8,9,11,19,21], they often exist as uniform arrays or pile-ups of long, straight dislocation segments. In contrast, at low temperatures, the $\langle c+a \rangle$ transitions cannot occur fast enough, leading to more normal evolution of dislocation densities, strengthening, and strain hardening, although now limited simply by the low temperature. Thus, the Pyr. II $\langle c+a \rangle$ dislocation transformations are responsible for the anomalous temperature dependence of the strengthening observed in the range of $\sim$130-293K [16,17], for the high hardening rate observed at 300K[9,14,18,19], and for the associated low ductility.

Discussion

The transitions identified here are intrinsic to Mg and occur without additional defects or spurious experimental conditions (such as electron beam heating). To prevent the undesirable transitions, strategies could be aimed at energetically stabilizing the easy-glide $\langle c+a \rangle$ core so as to shift the transition to higher temperatures, longer times, or slower strain rates. This may be possible by solute additions that pin the easy-glide $\langle c+a \rangle$ core and lower its energy. Quantitative models demonstrate that glide dislocations are pinned by favorable statistical fluctuations of the solute distribution[32], and the favorable fluctuations for the easy-glide $\langle c+a \rangle$ core will not simultaneously be favorable for the basal-dissociated core at the same position. New encouraging results[11,33,34] on Mg-3%Y alloys show substantially increased $\langle c+a \rangle$ activity and higher ductility, which may be due to increased stability of the easy-glide $\langle c+a \rangle$ by these solutes. Modeling of the interaction between alloying elements and the various dislocation cores found here, and analysis of the consequent effects on the stability of the Pyr. II $\langle c+a \rangle$ edge dislocation, would thus appear to be a useful direction to pursue. Our results also suggest that sufficiently small grain sizes could be favorable for ductility. If easy glide $\langle c+a \rangle$ dislocations exist long enough to fully traverse grains, then the undesirable transitions are avoided. Indeed, TEM observations in large grain materials show arrays of straight $\langle c+a \rangle$ dislocation segments[11,21] inside grains but particularly near grain boundaries[35], suggesting that the $\langle c+a \rangle$ are nucleated near grain boundaries but then only travel a short distance before transforming. In contrast, high ductility is achieved in Mg with micron-scale grain sizes[10]. Finally, the mechanism of the $\langle c+a \rangle$ transition and its consequent strength anomalies may not be unique to Mg; similar observations are seen in other hcp metals[7,17,20] (Cd,

Zn, etc.). Since the observed transition is intrinsic, results in immobile dislocations, and occurs at high rates, it may also provide the "unknown" pinning process invoked by Price[7] in one proposed mechanism aimed at rationalizing the observation of basal-oriented $\langle c + a \rangle$ dislocation loops.

In summary, use of a new DFT-validated MEAM potential in long-time MD studies reveals a rich set of intrinsic structural transitions of the key $\langle c + a \rangle$ dislocations in Mg that explain long-standing experimental puzzles and are responsible for low ductility in Mg. The easy-glide Pyr. II $\langle c + a \rangle$ undergoes thermally-activated, stress-dependent transitions into various lower-energy products lying on the basal plane. The dislocation structures are in good agreement with experimental observations, the differences among experiments are explained, the temperature range where the transition is operative agrees with experiments, and the product dislocations are immobile and so cause high strain hardening by serving as obstacles for all other dislocations, leading to low ductility. This new overall understanding opens opportunities for design of Mg-based alloys based on the mechanistic concept of energetically stabilizing the easy-glide $\langle c + a \rangle$ dislocations on the pyramidal II planes.

Acknowledgements

Author Contributions

Z.W. and W.A.C. designed the research, analysed the data, developed the model, discussed the results, and wrote the paper. Z.W. performed the molecular dynamics simulations.

Author Information

Reprints and permissions information is available at www.nature.com/reprints. The authors declare no competing financial interests. Correspondence and requests for materials should be

addressed to W.A.C.(william.curtin@epfl.ch).

[1] Miller, W. S. *et al.* Recent development in aluminium alloys for the automotive industry. *Materials Science and Engineering: A* **280**, 37–49 (2000). URL http://www.sciencedirect.com/science/article/pii/S092150939900653X.

[2] Kulekci, M. K. Magnesium and its alloys applications in automotive industry. *International Journal of Advanced Manufacturing Technology* **39**, 851–865 (2008). URL http://www.scopus.com/inward/record.url?eid=2-s2.0-55649125358&partnerID=40&md5=dd63e6ee9f7ab2c4afceb27245b1f2da.

[3] Heinz, A. *et al.* Recent development in aluminium alloys for aerospace applications. *Materials Science and Engineering: A* **280**, 102–107 (2000). URL http://www.sciencedirect.com/science/article/pii/S0921509399006747.

[4] Pollock, T. M. Weight loss with magnesium alloys. *Science* **328**, 986–987 (2010). URL http://www.sciencemag.org/content/328/5981/986.short.

[5] Hirth, J. P. & Lothe, J. *Theory of Dislocations* (John Wiley & Sons, 1982), 2 edn.

[6] Agnew, S. R. *Deformation mechanisms of magnesium alloys*, chap. 2, 63–104 (Woodhead Publishing Limited, 2012). URL http://www.scopus.com/inward/record.url?eid=2-s2.0-84893708167&partnerID=40&md5=096c32753aa346761c27c5e730a78c16.

[7] Price, P. B. Nonbasal glide in dislocation–free Cadmium crystals. II. the $(11\bar{2}2)\,[\bar{1}\bar{1}23]$ system. *Journal of Applied Physics* **32**, 1750–1757 (1961). URL http://scitation.aip.org/content/aip/journal/jap/32/9/10.1063/1.1728430.

[8] Stohr, J. F. & Poirier, J. P. Etude en microscopie electronique du glissement pyramidal $\{11\bar{2}2\}\,\langle 11\bar{2}3\rangle$ dans le magnesium. *Philosophical Magazine* **25**, 1313–1329 (1972). URL http://dx.doi.org/10.1080/14786437208223856.

[9] Obara, T., Yoshinga, H. & Morozumi, S. $\{11\bar{2}2\}\,\langle\bar{1}\bar{1}23\rangle$ slip system in magnesium. *Acta Metallurgica* **21**, 845–853 (1973). URL http://www.sciencedirect.com/science/article/pii/0001616073901417.

[10] Koike, J. *et al.* The activity of non-basal slip systems and dynamic recovery at room temperature

14

in fine-grained AZ31B magnesium alloys. *Acta Materialia* **51**, 2055–2065 (2003). URL `http://www.sciencedirect.com/science/article/pii/S1359645403000053`.

[11] Sandlöbes, S., Friák, M., Neugebauer, J. & Raabe, D. Basal and non-basal dislocation slip in Mg–Y. *Materials Science and Engineering: A* **576**, 61–68 (2013). URL `http://www.sciencedirect.com/science/article/pii/S0921509313002670`.

[12] Yang, Z., Chisholm, M. F., Duscher, G., Ma, X. & Pennycook, S. J. Direct observation of dislocation dissociation and Suzuki segregation in a Mg–Zn–Y alloy by aberration-corrected scanning transmission electron microscopy. *Acta Materialia* **61**, 350–359 (2013). URL `http://www.sciencedirect.com/science/article/pii/S1359645412007008`.

[13] Yu, Q., Qi, L., Mishra, R. K., Li, J. & Minor, A. M. Reducing deformation anisotropy to achieve ultrahigh strength and ductility in Mg at the nanoscale. *Proceedings of the National Academy of Sciences of the United States of America* **110**, 13289–13293 (2013). URL `http://www.ncbi.nlm.nih.gov/pmc/articles/PMC3746912/`.

[14] Geng, J., Chisholm, M. F., Mishra, R. K. & Kumar, K. S. The structure of $\langle c + a \rangle$ type dislocation loops in magnesium. *Philosophical Magazine Letters* **94**, 377–386 (2014). URL `http://dx.doi.org/10.1080/09500839.2014.916423`.

[15] Kitahara, T., Ando, S., Tsushida, M., Kitahara, H. & Tonda, H. Deformation behavior of magnesium single crystals in c-axis compression. *Key Engineering Materials* **345-346**, 129–132 (2007).

[16] Ando, S. & Tonda, H. Non-basal slips in magnesium and magnesium-lithium alloy single crystals. *Materials Science Forum* **350-351**, 43–48 (2000).

[17] Tonda, H. & Ando, S. Effect of temperature and shear direction on yield stress by $\{11\bar{2}2\}$ $\langle \bar{1}\bar{1}23 \rangle$ slip in HCP metals. *Metallurgical and Materials Transactions A - Physical Metallurgy and Materials Science* **33**, 831–836 (2002). URL `http://dx.doi.org/10.1007/s11661-002-0152-z`.

[18] Byer, C. M., Li, B., Cao, B. & Ramesh, K. T. Microcompression of single-crystal magnesium. *Scripta Materialia* **62**, 536–539 (2010). URL `http://www.sciencedirect.com/science/article/pii/S1359646209007702`.

[19] Syed, B., Geng, J., Mishra, R. K. & Kumar, K. S. [0001] compression response at room temperature of single-crystal magnesium. *Scripta Materialia* **67**, 700–703 (2012). URL `http://www.sciencedirect.com/science/article/pii/S1359646212004307`.

[20] Price, P. B. Pyramidal glide and the formation and climb of dislocation loops in nearly perfect zinc crystals. *Philosophical Magazine* **5**, 873–886 (1960). URL `http://www.informaworld.com/`

10.1080/14786436008238307.

[21] Agnew, S. R., Horton, J. A. & Yoo, M. H. Transmission electron microscopy investigation of $\langle c + a \rangle$ dislocations in Mg and α-solid solution Mg-Li alloys. *Metallurgical and Materials Transactions A* **33**, 851–858 (2002). URL http://dx.doi.org/10.1007/s11661-002-0154-x.

[22] Bettles, C. J., Gibson, M. A. & Zhu, S. M. Microstructure and mechanical behaviour of an elevated temperature Mg-rare earth based alloy. *Materials Science and Engineering: A* **505**, 6–12 (2009). URL http://www.sciencedirect.com/science/article/pii/S0921509308012768.

[23] Hidalgo-Manrique, P. *et al.* Origin of the reversed yield asymmetry in Mg-rare earth alloys at high temperature. *Acta Materialia* **92**, 265–277 (2015). URL http://www.sciencedirect.com/science/article/pii/S1359645415002293.

[24] Yoo, M. H., Agnew, S. R., Morris, J. R. & Ho, K. M. Non-basal slip systems in HCP metals and alloys: source mechanisms. *Materials Science and Engineering: A* **319–321**, 87–92 (2001). URL http://www.sciencedirect.com/science/article/pii/S0921509301010279.

[25] Edelin, G. & Poirier, J. P. Etude de la montée des dislocations au moyen d'expériences de fluage par diffusion dans le magnésium. *Philosophical Magazine* **28**, 1203–1210 (1973). URL http://dx.doi.org/10.1080/14786437308227994.

[26] Wu, Z., Francis, M. F. & Curtin, W. A. Magnesium interatomic potential for simulating plasticity and fracture phenomena. *Modelling and Simulation in Materials Science and Engineering* **23**, 015004 (2015). URL http://stacks.iop.org/0965-0393/23/i=1/a=015004.

[27] Henkelman, G. & Jónsson, H. Improved tangent estimate in the nudged elastic band method for finding minimum energy paths and saddle points. *Journal of Chemical Physics* **113**, 9978–9985 (2000). URL http://link.aip.org/link/?JCP/113/9978/1.

[28] Henkelman, G., Uberuaga, B. P. & Jónsson, H. A climbing image nudged elastic band method for finding saddle points and minimum energy paths. *Journal of Chemical Physics* **113**, 9901–9904 (2000). URL http://link.aip.org/link/?JCP/113/9901/1.

[29] Kocks, U. F., Argon, A. S. & Ashby, F. Thermodynamics and kinetics of slip. *Progress in Materials Science* **19**, 1–291 (1975). URL http://books.google.ch/books?id=4LI-pwAACAAJ.

[30] Devincre, B., Hoc, T. & Kubin, L. Dislocation mean free paths and strain hardening of crystals. *Science* **320**, 1745–1748 (2008).

[31] Bertin, N., Tomé, C. N., Beyerlein, I. J., Barnett, M. R. & Capolungo, L. On the strength of dislocation interactions and their effect on latent hardening in pure magnesium. *International Journal of Plastic-*

ity **62**, 72–92 (2014). URL http://www.sciencedirect.com/science/article/pii/S0749641914001326.

[32] Leyson, G. P. M., Curtin, W. A., Hector, L. G. & Woodward, C. F. Quantitative prediction of solute strengthening in aluminium alloys. *Nature Materials* **9**, 750–755 (2010). URL http://dx.doi.org/10.1038/nmat2813.

[33] Sandlöbes, S. *et al.* The relation between ductility and stacking fault energies in Mg and Mg–Y alloys. *Acta Materialia* **60**, 3011–3021 (2012). URL http://www.sciencedirect.com/science/article/pii/S1359645412001024.

[34] Sandlöbes, S. *et al.* Ductility improvement of Mg alloys by solid solution: Ab initio modeling, synthesis and mechanical properties. *Acta Materialia* **70**, 92–104 (2014). URL http://www.sciencedirect.com/science/article/pii/S1359645414000949.

[35] Kang, F., Liu, J. Q., Wang, J. T. & Zhao, X. The effect of hydrostatic pressure on the activation of non-basal slip in a magnesium alloy. *Scripta Materialia* **61**, 844–847 (2009). URL http://www.sciencedirect.com/science/article/pii/S1359646209004618.

[36] Plimpton, S. Fast parallel algorithms for short-range molecular dynamics. *Journal of Computational Physics* **117**, 1–19 (1995). URL http://www.sciencedirect.com/science/article/B6WHY-45NJN1B-3N/2/58aa2a309d2ebbbe60e0f417d398b0ef.

[37] Nosé, S. A molecular dynamics method for simulations in the canonical ensemble. *Molecular Physics: An International Journal at the Interface Between Chemistry and Physics* **52**, 255–268 (1984). URL http://www.informaworld.com/10.1080/00268978400101201.

[38] Nosé, S. A unified formulation of the constant temperature molecular dynamics methods. *Journal of Chemical Physics* **81**, 511–519 (1984). URL http://link.aip.org/link/?JCP/81/511/1.

[39] Hoover, W. G. Constant-pressure equations of motion. *Physical Review A* **34**, 2499–2500 (1986). URL http://link.aps.org/abstract/PRA/v34/p2499.

[40] Melchionna, S., Ciccotti, G. & Holian, B. L. Hoover NPT dynamics for systems varying in shape and size. *Molecular Physics: An International Journal at the Interface Between Chemistry and Physics* **78**, 533–544 (1993). URL http://www.informaworld.com/10.1080/00268979300100371.

[41] Faken, D. & Jónsson, H. Systematic analysis of local atomic structure combined with 3D computer graphics. *Computational Materials Science* **2**, 279–286 (1994). URL http://www.

17

sciencedirect.com/science/article/pii/0927025694901090.

[42] Liu, X.-Y., Adams, J. B., Ercolessi, F. & Moriarty, J. A. EAM potential for magnesium from quantum mechanical forces. *Modelling and Simulation in Materials Science and Engineering* **4**, 293 (1996). URL http://stacks.iop.org/0965-0393/4/i=3/a=004.

[43] Sun, D. Y. *et al.* Crystal-melt interfacial free energies in hcp metals: A molecular dynamics study of Mg. *Physical Review B* **73**, 024116–12 (2006). URL http://link.aps.org/doi/10.1103/PhysRevB.73.024116.

[44] Nogaret, T., Curtin, W. A., Yasi, J. A., Hector Jr, L. G. & Trinkle, D. R. Atomistic study of edge and screw $\langle c+a \rangle$ dislocations in magnesium. *Acta Materialia* **58**, 4332–4343 (2010). URL http://www.sciencedirect.com/science/article/pii/S1359645410002387.

[45] Ghazisaeidi, M., Hector Jr, L. G. & Curtin, W. A. First-principles core structures of $\langle c+a \rangle$ edge and screw dislocations in Mg. *Scripta Materialia* **75**, 42–45 (2014). URL http://www.sciencedirect.com/science/article/pii/S1359646213005708.

[46] Hartley, C. S. & Mishin, Y. Characterization and visualization of the lattice misfit associated with dislocation cores. *Acta Materialia* **53**, 1313–1321 (2005). URL http://www.sciencedirect.com/science/article/pii/S1359645404007062.

[47] Vitek, V. Theory of the core structures of dislocations in body-centered-cubic metals. *Crystalline Lattice Defects* **5**, 1–34 (1974).

[48] Peach, M. & Koehler, J. S. The forces exerted on dislocations and the stress fields produced by them. *Physical Review* **80**, 436–439 (1950).

[49] Chou, Y. T. Interaction of parallel dislocations in a hexagonal crystal. *Journal of Applied Physics* **33**, 2747–2751 (1962). URL http://scitation.aip.org/content/aip/journal/jap/33/9/10.1063/1.1702541.

[50] Teutonico, L. J. Dislocations in hexagonal crystals. *Materials Science and Engineering* **6**, 27–47 (1970). URL http://www.sciencedirect.com/science/article/pii/0025541670900753.

[51] Savin, M. M., Chernov, V. M. & Strokova, A. M. Energy factor of dislocations in hexagonal crystals. *Physica Status Solidi (a)* **35**, 747–754 (1976). URL http://dx.doi.org/10.1002/pssa.2210350240.

Methods

Reference 36-51 are for Methods section.

MD simulations

MD simulations are performed using LAMMPS[36]. Interatomic interactions between Mg atoms are described by an MEAM-type potential parametrized and validated in our earlier work[26] (see below). Various MD cell dimensions are tested with periodic boundary conditions applied only in the dislocation line (z) direction (see below). All dislocations are created at the center of the simulation cell using the anisotropic elastic Volterra displacement field[5] and subsequently relaxed with atoms within $2 \times$ cut off distance ($2r_c$) of the potential from the boundary fixed at the elastic displacement solution. In finite temperature simulations, atom positions are first scaled from T = 0 K using the finite-temperature lattice parameters, followed by initializing the atom velocities using a Gaussian distribution. A Nosé-Hoover thermostats[37–40] is used to maintain constant temperature. All energy minimizations are carried out using a conjugate gradient algorithm and atomic structures are identified using common neighbor analysis[41].

MEAM potential

Molecular Dynamics simulations have been hampered by a lack of valid interatomic potentials, with existing potentials [42,43] showing a menagerie of structures that do not glide on the Pyr. II plane[6,44]. In the current work, we use a newly developed MEAM-type interatomic potential[26] which has been validated to predict all observed glide dislocation cores in Mg in agreement with all available DFT computations and experiments. Extend Data Fig. 1 shows the $\langle \mathbf{c} + \mathbf{a} \rangle$ edge and screw dislocation core structures on pyramidal II planes as predicted by the MEAM potential[26] and DFT[45]. Dislocation core structures are visualized using both the component of the Nye tensor plot[46] and differential displacement plot[47]. The MEAM potential and DFT calculation predict similar core structures; both the edge and screw dislocations dissociate into partials of $1/2\langle \mathbf{c} + \mathbf{a} \rangle$ on Pyr. II planes with the partial dislocations having primarily pure edge or pure screw character and different partial core structures. For further details, see Ref[26].

"Climb"-like $\langle c + a \rangle$ edge dislocation transition

The $\langle c + a \rangle$ edge dislocation undergoes a "climb"-like transition from the easy-glide Pyr. II plane to the basal plane. This process, however, does not involve long-range atom diffusion. In our simulations, there are no vacancies - none are introduced at the start of the simulation and none are created during the simulation. Specifically, the simulation cell starts from a perfect hcp lattice, and the $\langle c + a \rangle$ dislocation is introduced using the anisotropic elastic Volterra displacement field with the total number of atoms conserved. During the simulations, no vacancy/interstitial pairs are formed outside the dislocation core region. The transition is atomistically complicated. Extended Data Fig. 3 shows the atom trajectories during the transition from Pyr. II $\langle c + a \rangle$ to basal $\langle c + a \rangle$ at 500 K. No vacancy/interstitial diffusion from the surrounding bulk into the dislocation core region is observed throughout the transition. Instead, the transition is accomplished by local atom rearrangement near the core region, which results in one partial climbing up and the other climbing down; this is a self-compensated process. This process may involve, or be interpreted as involving, some local vacancy/interstitial creation and motion, but such processes are not clearly revealed from the complicated atomic motions. But there is definitely no longer-range transport of material, and the process is thus entirely different from a traditional dislocation climb mechanism where vacancy/interstitial diffusion from the bulk occurs.

Equilibrium separation of the basal-dissociated partial $\langle 1/2c + p \rangle$ dislocations

The interaction force between the two basal dissociated partial dislocations can be calculated using the Peach-Koehler formula[48]

$$\mathbf{f} = (\boldsymbol{\sigma} \cdot \mathbf{b}) \times \boldsymbol{\xi} \tag{4}$$

where $\boldsymbol{\sigma}$ is the stress field produced by one of the partial, and $\mathbf{b}$ and $\boldsymbol{\xi}$ are the Burgers vector and line direction vector of the other partial. We use the right-handed Cartesian coordinate system with x_3 parallel to the dislocation line, x_2 normal to the basal plane and consider the two partials separated by distance d, as shown in Extended Data Fig. 4. The dislocation Burgers vector and line direction are $\mathbf{b} = [a/2, c/2, \sqrt{3}a/6]$ and $\boldsymbol{\xi} = [0, 0, 1]$. The force per unit length in the x_1 direction[5,49] is

$$f_1(d) = \sigma_{21}(d, 0)b_1 + \sigma_{22}(d, 0)b_2 + \sigma_{23}(d, 0)b_3 = \frac{1}{2\pi d}\left(K_e b_1^2 + K_n b_2^2 - K_s b_3^2\right) \tag{5}$$

where

$$K_e = \left(\bar{C}_{13} + C_{13}\right) \left[\frac{C_{44}\left(\bar{C}_{13} - C_{13}\right)}{C_{33}\left(\bar{C}_{13} + C_{13} + 2C_{44}\right)}\right]^{1/2} \tag{6}$$

$$K_n = \left(\bar{C}_{13} + C_{13}\right) \left[\frac{C_{44}\left(\bar{C}_{13} - C_{13}\right)}{C_{11}\left(\bar{C}_{13} + C_{13} + 2C_{44}\right)}\right]^{1/2} \tag{7}$$

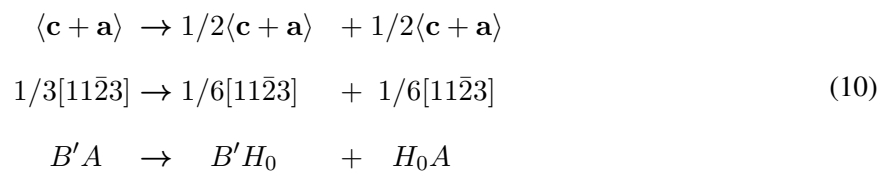$$K_s = \left[\frac{C_{11} - C_{12}}{2C_{44}}\right]^{1/2} \tag{8}$$

and

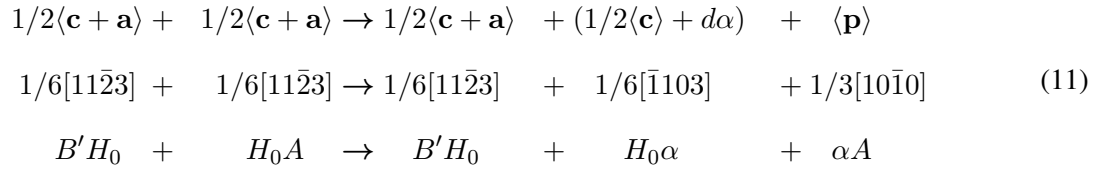$$\bar{C}_{13} = (C_{11}C_{33})^{1/2} \tag{9}$$

where C_{ij} are the elastic constants of the hexagonal crystal with x_3 as the **c**-axis. The equilibrium distance is determined by the balance between the repulsive force due to the partial dislocation interaction calculated in Eqn. 5 and the attractive configurational force γ_{I_1} due to the basal I_1 stacking fault. Using the calculated elastic constants and γ_{I_1} = 11.3 mJ/m^2 of the MEAM potential[26], the equilibrium separation is d = 37 nm. This suggests there is a thermodynamic driving force to increase the partial separation beyond the separation observed in the simulations. However, this separation process is kinetically difficult because it requires self-compensated climb between the two partials, i.e., nucleation of a vacancy/interstitial at one partial core and then migration of the vacancy/interstitial to the other. Thus, measured partial spacings could vary widely depending on conditions. In many experiments[8,9,11,19,21], $\langle \mathbf{c} + \mathbf{a} \rangle$ dislocations often appear as arrays of long, straight segments lying on the basal plane with no wide partial splitting observed. However, Geng et al.[14] reported that the stacking fault width varies widely (estimated from a few nm to a few tens of nm) for the $\langle \mathbf{c} + \mathbf{a} \rangle$ dislocation loops on the basal plane. The wide range of splitting might be associated with the dislocation loop configuration that has jogs and other defects that might facilitate nucleation of the necessary vacancies and interstitials.

Dislocation reaction during the $\langle \mathbf{c} + \mathbf{a} \rangle$ dislocation transition
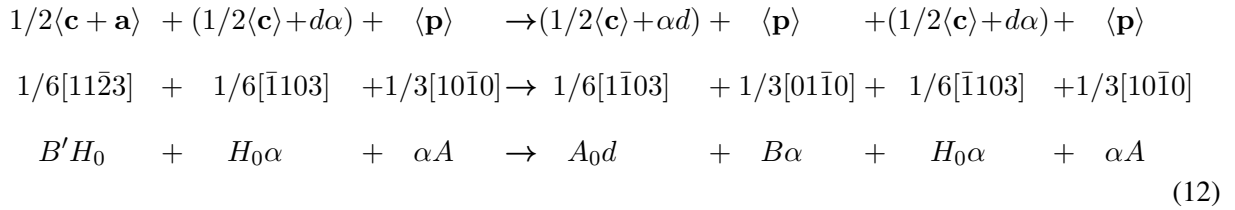
All simulations start from a $\langle \mathbf{c} + \mathbf{a} \rangle$ edge dislocation dissociated on Pyr. II planes as

$$\langle \mathbf{c} + \mathbf{a} \rangle \rightarrow 1/2\langle \mathbf{c} + \mathbf{a} \rangle + 1/2\langle \mathbf{c} + \mathbf{a} \rangle$$

$$1/3[11\bar{2}3] \rightarrow 1/6[11\bar{2}3] + 1/6[11\bar{2}3] \tag{10}$$
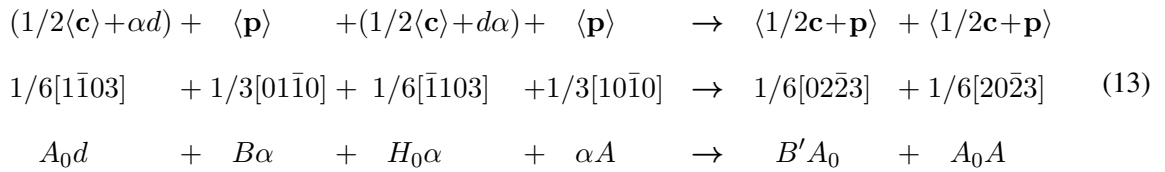
$$B'A \rightarrow B'H_0 + H_0A$$

where the Burgers vector notations are shown in Extended Data Fig. 5 following Hirth and Lothe[5]. In the low stress cases as shown in Extended Data Fig. 5a, a Shockley type partial dislocation $\langle \mathbf{p} \rangle$ is nucleated from one of the $1/2\langle \mathbf{c} + \mathbf{a} \rangle$ as following:
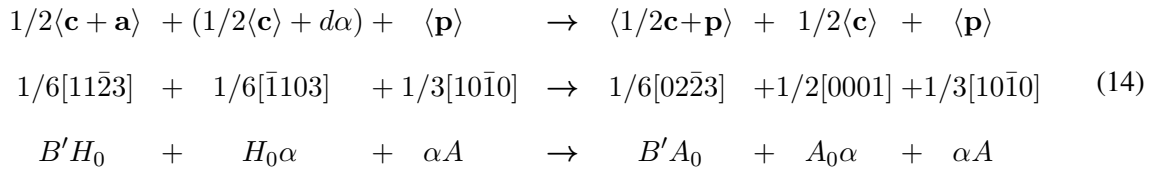
$$1/2\langle \mathbf{c}+\mathbf{a}\rangle + \; 1/2\langle \mathbf{c}+\mathbf{a}\rangle \to 1/2\langle \mathbf{c}+\mathbf{a}\rangle \; + (1/2\langle \mathbf{c}\rangle + d\alpha) \; + \; \langle \mathbf{p}\rangle$$

$$1/6[11\bar{2}3] + \quad 1/6[11\bar{2}3] \to 1/6[11\bar{2}3] \quad + \quad 1/6[\bar{1}103] \qquad + 1/3[10\bar{1}0] \qquad (11)$$

$$B'H_0 \; + \qquad H_0A \quad \to \quad B'H_0 \qquad + \qquad H_0\alpha \qquad + \quad \alpha A$$

A second Shockley partial is nucleated from the other $1/2\langle \mathbf{c} + \mathbf{a} \rangle$ as

$$1/2\langle \mathbf{c}+\mathbf{a}\rangle \; + (1/2\langle \mathbf{c}\rangle + d\alpha) + \; \langle \mathbf{p}\rangle \quad \to (1/2\langle \mathbf{c}\rangle + \alpha d) + \; \langle \mathbf{p}\rangle \qquad + (1/2\langle \mathbf{c}\rangle + d\alpha) + \; \langle \mathbf{p}\rangle$$

$$1/6[11\bar{2}3] \; + \; 1/6[\bar{1}103] \; +1/3[10\bar{1}0] \to 1/6[1\bar{1}03] \; + 1/3[01\bar{1}0] + \; 1/6[\bar{1}103] \; +1/3[10\bar{1}0]$$

$$B'H_0 \quad + \quad H_0\alpha \qquad + \quad \alpha A \quad \to \quad A_0d \qquad + \quad B\alpha \quad + \quad H_0\alpha \qquad + \quad \alpha A$$

$$(12)$$

Finally, the resulting partials in the above equation combine (αd annihilates with $d\alpha$) as

$$(1/2\langle \mathbf{c}\rangle + \alpha d) + \; \langle \mathbf{p}\rangle \qquad + (1/2\langle \mathbf{c}\rangle + d\alpha) + \; \langle \mathbf{p}\rangle \qquad \to \quad \langle 1/2\mathbf{c}+\mathbf{p}\rangle \; + \langle 1/2\mathbf{c}+\mathbf{p}\rangle$$

$$1/6[1\bar{1}03] \qquad + 1/3[01\bar{1}0] + \; 1/6[\bar{1}103] \quad +1/3[10\bar{1}0] \quad \to \quad 1/6[02\bar{2}3] \; + 1/6[20\bar{2}3] \qquad (13)$$

$$A_0d \qquad + \quad B\alpha \quad + \quad H_0\alpha \qquad + \quad \alpha A \quad \to \quad B'A_0 \quad + \quad A_0A$$

At intermediate stresses (see Extended Data Fig. 5b), the earlier nucleated Shockley partial dislocation $\langle \mathbf{p} \rangle$ glides away and the second partial dislocation is not nucleated. Following Eqn. 11, the dislocation reaction ($1/2\langle \mathbf{c} + \mathbf{a} \rangle$ reacts with $d\alpha$) can be described as following

$$1/2\langle \mathbf{c}+\mathbf{a}\rangle \; + (1/2\langle \mathbf{c}\rangle + d\alpha) + \; \langle \mathbf{p}\rangle \qquad \to \quad \langle 1/2\mathbf{c}+\mathbf{p}\rangle \; + \; 1/2\langle \mathbf{c}\rangle \; + \; \langle \mathbf{p}\rangle$$

$$1/6[11\bar{2}3] \quad + \quad 1/6[\bar{1}103] \quad + 1/3[10\bar{1}0] \quad \to \quad 1/6[02\bar{2}3] \; + 1/2[0001] +1/3[10\bar{1}0] \qquad (14)$$

$$B'H_0 \qquad + \qquad H_0\alpha \qquad + \quad \alpha A \quad \to \quad B'A_0 \quad + \quad A_0\alpha \quad + \quad \alpha A$$

At high stresses (see Extended Fig. 5c), the trailing Shockley partial dislocation $\langle \mathbf{p} \rangle$ is nucleated immediately following the leading partial. Following Eqn. 12, the dislocation reaction can be described as following

$$(1/2\langle \mathbf{c}\rangle + \alpha d) + \; \langle \mathbf{p}\rangle \qquad + (1/2\langle \mathbf{c}\rangle + d\alpha) + \; \langle \mathbf{p}\rangle \qquad \to \quad (1/2\langle \mathbf{c}\rangle + 1/2\langle \mathbf{c}\rangle) \qquad + \qquad \langle \mathbf{a}\rangle$$

$$1/6[1\bar{1}03] \quad + 1/3[01\bar{1}0] +1/6[\bar{1}103] \quad +1/3[10\bar{1}0] \to (1/2[0001]+1/2[0001]) \; +(1/3[01\bar{1}0]+1/3[10\bar{1}0])$$

$$A_0d \qquad + \quad B\alpha \quad + \quad H_0\alpha \qquad + \quad \alpha A \quad \to \quad (B'G_0 + G_0B) \qquad + \quad (B\alpha + \alpha A)$$

$$(15)$$
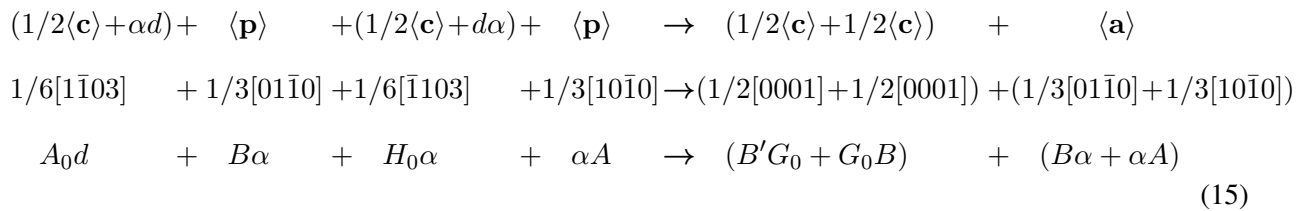
Transition time measurement and the effects of simulation cell size and boundary conditions

In the transition time measurement, the simulation cell has dimensions ($l_x \times l_y \times l_z$) of $\sim$30 nm $\times$ 30 nm $\times$ 2 nm with boundary atoms fixed at their elastic displacement solution. Transition rates are measured with twenty nominally identical simulations performed at each temperature and load, as shown by solid dots in Fig. 3. Two large simulation cells ($\sim$30 nm $\times$ 30 nm $\times$ 22 nm and $\sim$100 nm $\times$ 100 nm $\times$ 2 nm) with fixed boundary conditions and a large simulation cell ($\sim$200 nm $\times$ 200 nm $\times$ 2 nm) with free surface boundary conditions in the x and y directions are used to examine the effect of simulation cell size and boundary conditions on the observed transition. In these large scale simulations, transition rates are measured with ten nominally identical simulations and the results are shown in Fig. 3 by empty, half-filled and quarter-filled dots, respectively. Both the simulation cell size and the fixed boundary do not have significant effects on the transition rate, barrier or the transition type. As expected, the simulation size affects the final gliding distance of the $\langle \mathbf{a} \rangle$ dislocation after the transition but this is of no importance to the transition itself.

Statistical distribution of Pyramidal II $\langle \mathbf{c} + \mathbf{a} \rangle$ dislocation transition times

The thermally-activated transition process is a random process. The statistical distribution of measured transition times should thus follow the standard distribution for a Poisson random process. For a mean transition rate R, and corresponding mean transition time $\bar{t} = 1/R$, the cumulative probability distribution for the transition time should be

$$P(t) = 1 - e^{-Rt} = 1 - e^{-t/\bar{t}} \tag{16}$$

For the simulations shown in Extended Data Fig. 6, we have performed $N = 40$ nominally identical simulations to obtain N measures of the transition time, $t_1, ... t_N$. The cumulative probability distribution is obtained by ordering the transition times from smallest to largest, $t_1 < t_2 < \cdots < t_N$, and using the student t-test to assign the cumulative probability to the ith ordered transition time t_i as

$$P(t_i) = \frac{i - 0.3}{N + 0.4} \tag{17}$$

Extended Data Fig. 6 shows the transition probability distribution $P(t_i)$ vs. the normalized transition time $t_i/\bar{t}$ in semi-logarithmic form $-\ln(1 - P(t_i))$ vs. $t_i/\bar{t}$. In this form, linearity implies that the distribution follows the expected distribution of Eqn. 16 above. The results for all simulations

23

are linear over the central range of the distribution, with expected statistical noise in the tail of the distribution. These results thus show that the $\langle c + a \rangle$ dislocation transition is a thermally-activated random process.

Nudged elastic band calculation of the transition energy

Preliminary nudged elastic band[27,28] (NEB) calculations are performed to find the energy barrier to reach the kinetically-limiting intermediate transition state. The NEB calculations use 16 images and a simulation cell of $\sim$30 nm $\times$ 30 nm $\times$ 2 nm with boundary atoms fixed at their elastic displacement solution. However, because the transition process is very complex, involving complicated atom displacement on the scale of the lattice parameter and non-uniform core structures along the dislocation line, convergence (e.g., maximum force $< 10^{-3}$ eV/Å) of the NEB calculations has not yet been achieved. Our preliminary NEB calculations, although not absolutely converged, do provide a good estimate of the T = 0 K barrier of $\sim$0.6 eV. This is presumably an upper bound, and consistent with the value of $\sim$0.5 eV estimated from our direct transition time measurements in MD simulations. Differences between the two are also expected since the NEB calculations give the energy barrier at T = 0 K and the simulations are probing the free energy barrier at finite T, and the two can differ due to entropy effects.

Calculation of pyramidal II $\langle c + a \rangle$ dislocation energy

The dislocation energy prefactor K for the edge and screw $\langle c + a \rangle$ dislocations on Pyr. II planes[50,51] are

$$K_{edge} = b^2 \frac{\lambda^2 C_{33} + C_{13}}{1 + \beta^2} \left[\frac{C_{44} \left(\lambda^2 C_{33} - C_{13} \right)}{C_{33} \left(\lambda^2 C_{33} + C_{13} + 2C_{44} \right)} \right]^{1/2} \left(1 + \frac{\beta^2}{\lambda^2} \right) \qquad (18)$$

and

$$K_{screw} = b^2 \left[\frac{\left(C_{11} - C_{12} \right) C_{44}}{2} \right]^{1/2} \qquad (19)$$

where b is the Burgers vector of the $\langle c + a \rangle$ dislocation, and

$$\lambda^2 = \left(\frac{C_{11}}{C_{33}} \right)^{1/2} , \text{ and } \beta = \frac{c}{a} \qquad (20)$$

Extended Data Fig. 7 shows the dislocation energy for the screw $\langle c + a \rangle$ dislocation lying on the Pyr. II plane along with the various edge $\langle c + a \rangle$ dislocations, and the above analytical values

for the scaling of the energy. As expected, the coefficient K is smaller than that for the edge dislocation and the total energy including any core interactions is also lower. This is important because it shows that the dislocations in an initial sample under zero load will tend to relax toward the screw orientation, minimizing the number of edge segments that might otherwise transform into the immobile basal-oriented structures. Under loads, the dislocations will bow-out in between any pinning points and create more edge-like segments, which can then transform into one of the structures revealed here by MD. This rationalizes why the transformed structures are not widely observed in as-fabricated, well-annealed materials but can proliferate under applied loads.

In addition, the screw $\langle \mathbf{c} + \mathbf{a} \rangle$ dislocation dissociates into two partials screw $1/2\langle \mathbf{c} + \mathbf{a} \rangle + 1/2\langle \mathbf{c} + \mathbf{a} \rangle$ on Pyr. II plane (see Extended Data Fig. 1). This makes cross-slip of the $\langle \mathbf{c} + \mathbf{a} \rangle$ between Pyr. II and Pyr. I planes very easy at room temperature, which we have previously reported in MD simulations[26]. This easy cross-slip may facilitate operation of the loop creation mechanism proposed by Price[7]. Nevertheless, the screw $\langle \mathbf{c} + \mathbf{a} \rangle$ dislocation has lower energy on Pyr. II planes than on Pyr. I planes and it glides primarily on Pyr. II planes.

Dislocation glide behavior under shear loading

In the study of dislocation glide behavior, shear stress is created by applying forces on atoms within $2r_c$ of the top and bottom y-surfaces. The reported shear stress value is calculated based on the applied force divided by the area ($l_x \times l_z$). Extended Data Fig. 8 shows the motion of the various dislocations under applied resolved shear stresses on the Pyr. II $\langle \mathbf{c} + \mathbf{a} \rangle$ plane (a-c) and prism plane (d) at 300 K in both positive and negative directions. In (a-c), the direction of shear in the first column is equivalent to compression in $\mathbf{c}$-axis/tension in $\mathbf{a}$-axis while in the second column the direction is equivalent to tension in $\mathbf{c}$-axis/compression in $\mathbf{a}$-axis. The initial $\langle \mathbf{c} + \mathbf{a} \rangle$ dislocation is mobile, moving at stresses of ~11-13 MPa but with a small dependence on the direction of the applied shear; this is a non-Schmid effect and has recently been deduced to exist in Mg via analysis of experiments on polycrystals using crystal plasticity[23]. The $\langle \mathbf{c} \rangle$ dislocation dissociated on basal plane also exhibits a dependence on the direction of the applied stress; partial $\langle \mathbf{a} \rangle$ dislocation is nucleated at applied stresses of 503 and 464 MPa.

Extended Data

/Users/zxwu/workspace/mg_mechanics/submit_msmse/revision/figure_8.pdf

Extended Data Figure 1: Pyramidal II $\langle c + a \rangle$ edge and screw dislocation core structures predicted by the MEAM potential and DFT as visualized by the component of the Nye tensor and differential displacement plots.

./pic/gp/transition_type-crop.pdf

Extended Data Figure 2: Distribution of pyramidal $\langle \mathbf{c} + \mathbf{a} \rangle$ edge dislocation transition type at different applied stresses. At no or low applied stresses, basal $\langle \mathbf{c} + \mathbf{a} \rangle$ is dominant while partial $\langle \mathbf{a} \rangle$ and $\langle \mathbf{c} \rangle$ or full $\langle \mathbf{a} \rangle$ and $\langle \mathbf{c} \rangle$ dislocations are dominant at high applied stresses.

./pic/jpg/eca_s_500k_10_traj_0040.jpg

Extended Data Figure 3: Atom trajectory during transition from pyramidal II $\langle \mathbf{c} + \mathbf{a} \rangle$ to basal $\langle \mathbf{c} + \mathbf{a} \rangle$ at 500 K. Each while line traces individual atom trajectory during the transition.

./pic/tex/hcp_disl_ss/c_unit_cell_ss_ca-crop.pdf

Extended Data Figure 4: Schematics and coordinate system for $\langle c + a \rangle$ dislocation transition. $\langle c + a \rangle$ edge dislocation dissociated on pyramidal II plane climb-dissociates to basal plane.

Extended Data Figure 5: Dissociation details of the easy glide Pyr. II $\langle \mathbf{c}+\mathbf{a} \rangle$ into basal dissociated products as observed during long-time MD simulations, for (a) zero, (b) moderate, and (c) high compressive stresses normal to the Pyr. II plane. Dislocation cores are indicated by the symbol "⊥".

./pic/gp/random_process-crop.pdf

Extended Data Figure 6: Transition probability distribution for random processes.

Extended Data Figure 7: Energy of $\langle \mathbf{c} + \mathbf{a} \rangle$ dislocations calculated within a cylindrical region of radius r. (a) Schematics showing the total dislocation energy consisting of near core energy E_{struc} and far field elastic energy $K \ln (r/r_{min})$, where $r_{min} \approx 6b = 6|\mathbf{c} + \mathbf{a}|$. (b) The 4 dislocation energies (top to bottom) correspond to the $\langle \mathbf{c} + \mathbf{a} \rangle$ edge dislocation on pyramidal II plane, edge $\langle \mathbf{c} \rangle$ and $\langle \mathbf{a} \rangle$ in close proximity, $\langle \mathbf{c} + \mathbf{a} \rangle$ edge dislocation climb-dissociated on basal plane, and $\langle \mathbf{c} + \mathbf{a} \rangle$ screw dislocation on pyramidal II plane, respectively. The edge dislocations with different core configurations have different energy density within r_{min} but the same far field elastic energy scaling K. The screw dislocation has both lower energy within r_{min} and lower elastic energy prefactor than all the edge dislocations. The analytical energy prefactor K (the slope) from the anisotropic elastic solution are also shown.

Extended Data Figure 8: Glide behavior of the various dislocations under resolved shear stresses (directions indicated) at 300K. (a) easy glide Pyr. II $\langle \mathbf{c} + \mathbf{a} \rangle$ at $\sim$13 and 11 MPa with a distinct directional dependence; (b) glide of the basal-dissociated $\langle \mathbf{c} + \mathbf{a} \rangle$ but at very high stresses $\sim$330 MPa; (c) glide of the $\langle \mathbf{a} \rangle$ dislocation away from the remaining $\langle \mathbf{c} + \mathbf{a} \rangle$ product at $\sim$119 MPa leaving an immobile $\langle \mathbf{c} \rangle$ and reaction of $\langle \mathbf{a} \rangle$ and $\langle \mathbf{c} \rangle$ forming the basal $\langle \mathbf{c} + \mathbf{a} \rangle$ dislocation; (d) nucleation of partial $\langle \mathbf{a} \rangle$ dislocations at 400-600 MPa from the immobile basal-dissociated $\langle \mathbf{c} \rangle$ dislocation.